Materialia 8 (2019) 100473 (13 pages)

Thermodynamic and Kinetic Behavior of Low-Alloy Steels: An Atomic Level Study Using an Fe-Mn-Si-C Modified Embedded Atom Method (MEAM) Potential

I. Aslam[a,b], M. I. Baskes[c,d], D. T. Dickel[a], S. Adibi[a,b] B. Li[e], H. Rhee[a,b], M. Asle Zaeem[f,g], M. F. Horstemeyer[a,b]

[a] Department of Mechanical Engineering, Mississippi State University, Mississippi State, MS 39762, USA

[b] Center for Advanced Vehicular Systems, Mississippi State University, Starkville, MS 39759, USA

[c] Office of Research and Economic Development, Mississippi State University, Mississippi State, MS 39762, USA

[d] Los Alamos National Lab, Los Alamos, NM 87545, USA

[e] Department of Chemical and Materials Engineering, University of Nevada, Reno, 89557, USA

[f] Department of Materials Science and Engineering, Missouri University of Science and Technology, Rolla, MO 65409, USA

[g] Department of Mechanical Engineering, Colorado School of Mines, Golden, CO 80401, USA

Abstract

A quaternary element Modified Embedded Atom Method (MEAM) potential comprising Fe, Mn, Si, and C is developed by employing a hierarchical multiscale modeling paradigm to simulate low-alloy steels. Experimental information alongside first-principles calculations based on Density Functional Theory served as calibration data to upscale and develop the MEAM potential. For calibrating the single element potentials, the cohesive energy, lattice parameters, elastic constants, and vacancy and interstitial formation energies are used as target data. The heat of formation and elastic constants of binary compounds along with substitutional and interstitial formation energies serve as binary potential calibration data, while substitutional and interstitial pair binding energies aid in developing the ternary potential. Molecular dynamics simulations employing the developed potentials predict the thermal expansion coefficient, heat capacity, self-diffusion

coefficients, and stacking fault energy for steel alloys comparable to those reported in the literature.

Keywords: MEAM; first-principles; iron alloys; manganese; silicon

Corresponding Author: Imran Aslam.

Corresponding Author Email: ia31@msstate.edu

1.1 Introduction

The desire for increased fuel efficiency and reduced emissions without sacrificing safety is as much of a concern with automotive industries as it ever has been [1–3]. One of the approaches to achieving these goals is to improve the strengths of materials while reducing their weight, especially in steel alloys, so that lightweighting could be attained. Despite desirable material characteristics, high strength steels have limited fabrication capability due to deformation resistance that causes tooling wear [4]. Therefore, the challenge lies to perform compositional design of high strength alloys in a manner that decreases the weight, retains workability, but generates the required strength after fabrication [5]. Recently, the concept of third generation high strength steels, also known as 3G advanced high strength steels or 3G AHSSs, has attracted a lot of attention [6–9]. The 3G AHSSs possess greater strengths than the first generation high strength steels, but avoid the high costs of second generation high strength steels [10]. Thus, superior properties combined with affordability in the automotive industry has been the primary consideration of developing 3G AHSSs. One of the promising strategies to design and make 3G AHSSs is a quenching and partitioning method [11] in which austenite is stabilized through diffusion of carbon from supersaturated martensite to austenite, and thus formation of brittle carbides is suppressed.

To facilitate the development of 3G AHSSs, multiscale hierarchical simulation and modeling has been used to investigate the processing-microstructure-property relationship of these materials [12], which is critical to enable progress in the design of new AHSSs. One of the key challenges in multiscale modeling is to bridge individual length scales through proper transfer of information between electronic, atomistic, microscale,

mesoscale, and macroscales. Most AHSSs are multicomponent systems. It is necessary then to develop interatomic potentials that allow experimentally-tethered computer simulations to capture the time-scale and length-scale physics of 3GAHSS such that the lower length-scale mechanisms can be better understood and their influence in higher length scale models can be incorporated to design fast, inexpensive processing routes resulting in the desired microstructure [13].

Atomistic simulations at the lower length scales can bridge the gap in comprehending and quantifying the structure-property relationships. Accurate representation of atoms at the lower length scales can be provided by first-principle calculations but at the cost of either large simulation times or requiring extensive computational resources. In order to conduct any realistic simulation of alloy systems, a large number of atoms are imperative to consider and therefore, leave quantum methods impractical to use. However, semi-empirical interatomic potentials enabling accurate atomistic simulations present themselves as an alternative solution that can handle large alloy systems within a reasonable computational expense.

Daw and Baskes [14] developed the Embedded Atom Method (EAM), which has been used extensively as a semi-empirical atomistic potential for studying metals, covalent materials, and impurities [15–17]. The EAM formulation was later modified (MEAM) [18] to integrate angular dependencies of electron density and a number of single element and alloy potentials were generated using the updated formalism. Exploring the silicon-nickel alloys and interfaces [19], and tensile debonding of an aluminum-silicon interface [20] are among the few examples of the updated potentials applicability. Later, Lee and Baskes [21] improved the MEAM potential to account for the second nearest-neighbor (2NN MEAM)

interactions. The 2NN MEAM formalism has been applied to capture Body Centered Cubic (BCC) metals (Fe, Cr, Mo, W, V, Nb, Ta) [22–24], Face Centered Cubic (FCC) metals (Cu, Ag, Au, Ni, Pd, Pt, Al, Pb) [25,26], Hexagonal Close Packed (HCP) metals (Mg, Ti, Zr, Zn) [27–31], metals with complex structures (Mn) [32], and covalently bonded elements (H, C, Si, Ge, N) [33–37]. In addition, binary systems have been used to study lattice defects (Fe-H) [36], structure-property relationships [38], interstitial interactions with vacancies and dislocations (Fe-C, Fe-N) [37,39], and mechanical and deformation properties (Fe-Mn) [32].

Ternary potentials pose a much greater challenge than binary potentials simply due to a lack of robust experimental data and fewer calibration parameters. Some of the recent examples of ternary applications include garnering average diffusivities of ternary alloys (Fe-Cr-Ni) [40], atomistic mechanisms for tensile fracture (Ti-Al-N) [41], nucleation kinetics of carbides and nitride (Fe-Ti-C, Fe-Ti-N) [42], modeling of a wide class of Mg alloys containing Zn (Mg-Al-Zn) [29], and structural properties of gold-silica interfaces (Au-Si-O) [43]. The greatest challenge for any interatomic potential is the multi-component system containing more than three elements. Of the two reported higher order potentials in the NIST repository [44], only the one by Jelinek *et al.* [45] has been generated using the MEAM potential.

The current study will focus on developing a quaternary element MEAM potential for low-alloy steels with constituent elements of Fe, Mn, Si, and C. The calibration will be performed to produce single, binary, and ternary element data garnered from first-principles calculations and experiments. For binary calibrations, all possible binary interactions will be considered whereas only the imperative ternary interactions will be

evaluated. Validation testing to elucidate the applicability of the potential to capture thermodynamic and kinetic behavior of low-alloy steels will conclude the present study.

1.2 Single Element Interatomic Potential Development

The atomistic potential development for Fe alloys will follow a multiscale hierarchical modeling paradigm defined by Integrated Computational Materials Engineering (ICME) [46]. Since an accurate representation of the kinetics, thermodynamics, and thermomechanical response is required to capture the low-alloy steels, we calibrate the MEAM potential that can reproduce the fundamental properties of the elements. The calibration data for the interatomic potential will first rely on experimentally observed values and additional information will be collected from the lower length scale *ab-initio* calculations that can provide reliable measure of the forces on individual atoms.

1.2.1 First-Principle Calculations

The ground state energies for Fe, Mn, Si, and C are evaluated using first-principle calculations based on the Density Functional Theory (DFT). Vienna *Ab-initio* Simulation Package (VASP) code is employed to perform the calculations using the Projector Augmented-Wave (PAW) pseudo-potential and the exchange-correlation effects are treated by the Generalized Gradient Approximation (GGA) as parameterized by Perdew *et al.* [47]. To ensure energy convergence, the cut-off energy for the planewave basis of 500 eV and the gamma centered Monkhorst-Pack [48] k-point grid of 16 × 16 × 16 are used. In addition, all single element calculations consider spin polarization to account for

magnetism. For each element, the energy-volume curves of the most stable (lowest energy) structure is determined, and in addition, at least two more crystal structures are probed.

1.2.2 MEAM Potential Parameters (Energy Versus Lattice Spacing)

In order to simulate the dynamics of a large number of atoms and molecules within a reasonable timeframe to reveal macroscopic material properties, we need a transition from the quantum to the atomic length scale. As such, a 2NN MEAM [21] potential that incorporates angular dependence of the electron density into the EAM potential and considers second nearest-neighbor interactions is used for the present study, and the full-description of the formulation can be found in the appendix [45]. Finally, the Large-scale Atomic/Molecular Massively Parallel Simulator (LAMMPS) is employed for the atomistic simulations, which is used with the MEAM parameter calibration tool [49,50] for parameter calibration.

The MEAM potential parameters for Fe, Mn, Si, and C are listed in Table B.1 with BCC, FCC, Diamond Cubic (DC), and DC as the reference structures, respectively. These parameters are also available in the NIST interatomic potentials repository [44]. The first step towards the parameter calibration is to compare the relative stability of the energy-volume curves produced by the MEAM potential with the DFT results at 0K. Figure 1.1 illustrates the energy versus lattice spacing of at least three crystal structures for Fe, Mn, Si, and C. The new MEAM potential parameters correctly capture the most stable structures for Fe (BCC), Mn (α-Mn), Si (DC), and C (DC), and the relative stability of supplemental structures. The c/a ratio used in hcp packing is 1.633 for secondary or tertiary HCP structures of Fe and Mn. As recorded in Table 1.1, the cohesive energies and lattice parameters of the lowest energy structures are very similar to the experimental results.

Since MEAM potential requires a reference structure to describe the pair-potential, the lowest energy crystalline structures for Fe, Si, and C are also used to prescribe their reference structures. The stable, low temperature structure for Mn (α-Mn) is described by a 58 atom complex configuration that cannot easily specify the pair interaction for Mn. Therefore, FCC is chosen as the reference structure for Mn, and the MEAM parameters are adjusted such that α-Mn is the most stable structure. Lastly, the A15 crystal structure, which often lies close to the ground state, is probed for each single element to ensure that A15 is less stable than most stable crystalline structure of each element. The energy relative to the ground state of A15 per atom in eV is 0.074, 0.254, 0.534, and 4.622 for Fe, Mn, Si, and C, respectively.

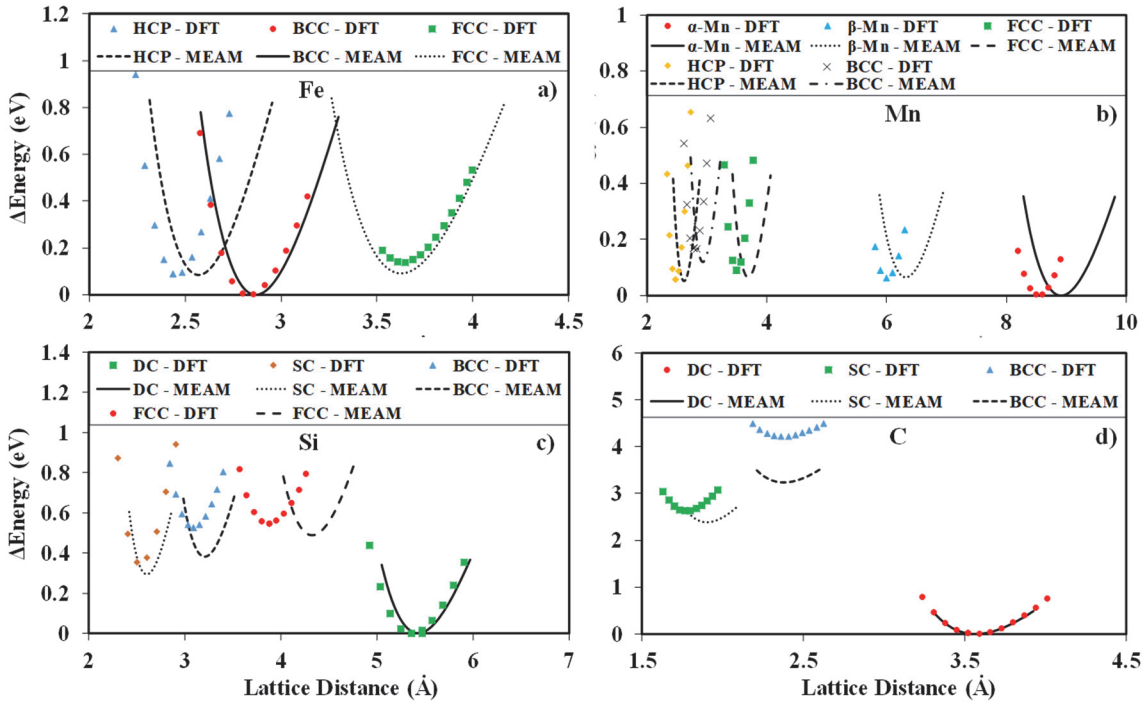

Figure 1.1 Relative energy versus lattice distance curves for a) Fe, b) Mn, c) Si, d) C. At least two crystalline structures are probed in addition to the ground states of body centered cubic (Fe), α-Mn (Mn), and diamond cubic (Si and

C) for each element using DFT and captured by the present MEAM potential.

Table 1.1 Lattice parameter and cohesive energy of stable crystal structures of Fe, Mn, Si, and C. Results produced by the MEAM potential match the experimental observations by construction.

Elements	Crystal Structure	Lattice Parameters (Å)			Cohesive Energy (eV/atom)		
		MEAM	Exp.	DFT	MEAM	Exp.	DFT
Fe	BCC	2.867	2.867[a]	2.835	4.28	4.28[a]	4.98
Mn	α	8.911	8.914[b]	8.54	2.92	2.92[a]	3.876
	β	6.32	6.315[b]	6.3	0.065*	-	0.062*
Si	DC	5.43	5.43[a]	5.473	4.63	4.63[a]	4.605
C	DC	3.567	3.567[c]	3.573	7.346	7.346[d]	7.85

* Energy relative to cohesive energy of α-Mn.

[a] [51]

[b] [52]

[c] Reference 21 as reported by [53]

[d] [54]

1.2.3 Vacancy Formation Energy

The energy cost required for the formation of a single vacancy (E_f^{Vac}) in the bulk of the lowest energy structure of each element is defined using the following equation:

$$E_f^{Vac} = E_{Total} - E_{Bulk}\left(\frac{N-1}{N}\right) \quad (0.1)$$

where N is defined as the total number of atoms comprising the perfect bulk, E_{Total} is the total relaxed energy of the bulk with a single vacancy (containing $N - 1$ total number of

atoms), and E_{Bulk} is the total relaxed energy of a perfect bulk system. The box dimensions are identical for the bulk with and without the defect. For the *ab-initio* calculations, the bulk dimensions used for the BCC and DC systems is a 4 × 4 × 4 primitive cell, 3 × 3 × 3 for the FCC system, but 1 × 1 × 1 for α-Mn due to the fact that the primitive cell contains 58 atoms and is fairly representative of the bulk. The bulk size incorporated in MEAM is a 5 × 5 × 5 primitive cell for BCC and DC, 4 × 4 × 4 for FCC, and 2 × 2 × 2 for α-Mn.

Table 1.2 compares the formation energies of a single vacancy using the MEAM potential for Fe (BCC), Mn (α-Mn), Si (DC), and C (DC) with experiment and DFT calculations. The interatomic potentials for Fe, Si, and C accurately reflect experimental observed energies and DFT results. A maximum deviation of 43% from the DFT results is observed for vacancy formation in Mn but is lower for the other elements. (Note that there is a difference between the DFT results and experiments as well!) Vacancy formation for α-Mn was calculated using DFT and the MEAM potential by creating a vacancy in each one of the four crystallographically inequivalent sites and averaging the results. Since the t_1 MEAM parameter directly controls vacancy formation energy, a compromise was achieved where the MEAM parameter was not abnormally large (>50), and the formation energy was positive for all four sites.

Table 1.2 Formation energy of a single vacancy predicted by MEAM parameters for Fe, Mn, Si, and C compared to experiment, DFT, and literature values. Difference is between MEAM and experiment (when known) or DFT.

	Vacancy Formation Energy (eV)				
Elements	MEAM	Experimental	DFT	Literature	% Diff.
Fe	1.53	1.53[a]	2.2	1.65[c]	0

Si		3.62	3.6[b]	3.63	3.56[d], 3.67[e]	0.6
C		6.63	-	6.63	3.35[f]	0
Mn	FCC	2.88	-	2.38	-	21
	α-Mn	1.34	-	2.33	0.9 – 1.2[g]	43

[a] [55]

[b] [56]

[c] MEAM value by Jelinek *et al.* [45]

[d] MEAM results by Timonova *et al.* [57]

[e] MEAM results by Ryu *et al.* [58]

[f] MEAM value by Lee *et al.* [33]

[g] MEAM results by Kim *et al.* [32], Semi-empirical model [59,60]

1.2.4 Self-Interstitial Formation Energy

The self-interstitial is another type of point defect and the formation energy for a single self-interstitial defect, E_f^{Int}, is evaluated by the following equation:

$$E_f^{Int} = E_{Total} - E_{Bulk}\left(\frac{N+1}{N}\right) \tag{0.2}$$

where N represents the total number of atoms in a defect-free bulk, E_{Total} is the total relaxed energy of the bulk with an extra atom of the same element placed at an interstitial location, and E_{Bulk} is the total relaxed energy of the bulk with a perfect crystalline lattice structure. Because we are most interested in Fe-based alloys, five distinct interstitial positions are investigated for BCC Fe: tetrahedral, octahedral, [100] split, [110] split, and the [111] split. Only the [110] split is evaluated for the diamond cubic structures of Si and C. Since α-Mn has a complex crystal structure, simulating an interstitial in the stable bulk

is more complicated and is not presented here. The bulk structures' dimensions for BCC and DC are the same as in the previous section.

The results for the self-interstitial formation energy captured by the MEAM potential in comparison to DFT are listed in Table 1.3. DFT results indicate that the [110] split is the most stable interstitial configuration for BCC Fe, and the potential accurately captures the relative stability of the five interstitials considered. In general, the MEAM potential results are within 10% of the DFT or literature results. The MEAM parameters are specifically adjusted to ensure that of the two types of point defects, vacancies have a lower formation energy than interstitials in the bulk of the element.

Table 1.3 Interstitial formation energy for Fe, Si, and C determined by MEAM potential in comparison with DFT and literature values. Various interstitial positions are inspected for Fe, and the MEAM potential accurately predicts [110] split as the most stable interstitial.

Elements	Interstitial Positions	Interstitial Formation Energy (eV)			% Diff.*
		MEAM	DFT	Literature	
Fe	Octahedral	4.94	4.9	5.0[a]	0.8
	Tetrahedral	4.35	4.0	4.2[a]	8.8
	[100] Split	4.91	-	4.8[a]	2.3
	[111] Split	4.37	-	4.9[a]	10.8
	[110] Split	3.61	3.6	3.9[a]	0.3
Si	[110] Split	3.88	3.65	3.7[a]	6.3
C	[110] Split	14.1	13.6	12.7[b]	3.7

* Percent difference calculated w.r.t. DFT (when known) or literature results.

[a] MEAM values obtained from Jelinek *et al.* [45]

[b] MEAM results by Lee [33]

1.2.5 Elastic Constants

By independently distorting the lattice in six different directions and using the force response, a stress-strain relationship is evaluated to provide the elastic constants of the material. Table 1.4 details the results of the MEAM calibration in comparison to the experimental and DFT values. The elastic constants evaluated for the DC structure of Si and C include relaxation of internal structures. For Fe, Si, and C, the MEAM potential and experimental elastic constants agree exactly by construction. However, due to a lack of robust experimental data available for Mn, certain assumptions were made. Initially, the MEAM potential elastic constants for FCC Mn were calibrated to replicate the DFT results but the resultant elastic constants for α-Mn, especially the bulk modulus, was twice as high as the experimental observations. To rectify the situation, we employed a technique similar to Kim *et al.* [32] where the calibration target was set to half the FCC elastic constants. Consequently, the bulk modulus of α-Mn was captured to be within the experimental range and specifically, the more recent observations.

Table 1.4 Elastic constants calculated for Fe, Mn, Si, and C. Difference between MEAM potential and experimental observations are given except when otherwise noted.

Elements	Elastic Constants	MEAM	Experimental	DFT	Literature	% Diff.
Fe	B (GPa)	168	168[a]	161	166[e]	0
	C′ (GPa)	48	48[a]	56.5	43.5[e]	0
	C_{44} (GPa)	117	117[a]	68	125[e]	0

α-Mn	B (GPa)	150	60 – 158[b]	-	134[f]	0
	C′ (GPa)	86	-	-	68.5[f]	25[*]
	C_{44} (GPa)	45	-	-	44[f]	2.3[*]
Mn (FCC)	B (GPa)	202	-	277	-	27[ϒ]
	C′ (GPa)	128	-	79	-	62[ϒ]
	C_{44} (GPa)	123	-	158	-	22[ϒ]
Si	B (GPa)	98	98[c]	100	98[e]	0
	C′ (GPa)	51	51[c]	49	49[e]	0
	C_{44} (GPa)	79	79[c]	77	76[e]	0
C	B (GPa)	442	442[d]	490	422[g]	0
	C′ (GPa)	476	476[d]	485	296[g]	0
	C_{44} (GPa)	577	577[d]	619	489[g]	0

$B = (C_{11} + 2C_{12})/3$; $C' = (C_{11} - C_{12})/2$

* Percent difference calculated w.r.t. literature results.

ϒ Percent different calculated w.r.t. DFT results divided by half (see text for more information)

[a] [51]

[b] [61–64]

[c] [65]

[d] [66]

[e] Calculated using parameters by Jelinek *et al.* [45]

[f] MEAM results from Kim *et al.* [32]

[g] Values reported using MEAM-BO calibration by Mun *et al.* [67]

1.3 Binary and Ternary Element Interatomic Potential Development

Similar to single element potential development, a binary and ternary interatomic potential will use DFT results to garner pertinent information that can be upscaled to the atomistic length scale as calibration data for the MEAM potentials. Experimental values will take precedence as the calibration targets while *ab-initio* results will provide information that is not found from experiments. All the binary and ternary element calculations consider spin polarization to account for magnetization. The final MEAM parameters obtained for the binary pairs, X – Y, are listed in Table B.2. For the ternary potentials, the screening parameters involving all three atoms are the only six parameters available for calibration and are recorded in Table B.3. The notation used to describe the screening parameters, C_{X-Y-Z}^{max} and C_{X-Y-Z}^{min}, is consistent with LAMMPS where X-Y-Z denotes atom Z screening atoms X and Y.

1.3.1 Heat (Enthalpy) of Formation

The first step towards binary potential development entails obtaining the energy-volume curve for all the binary combinations using at least four crystalline structures: B_1 (rock salt), B_2 (BCC equivalent), B_3 (DC equivalent), and L_{12} (FCC equivalent). The importance of evaluating the aforementioned structures stems from the fact that any of the four can be used as a reference structure to describe the pair potential, $\phi(R_{ij})$, during binary potential development and thereby, provide a robust calibration. In addition, the equilibrium energy and lattice parameters of experimentally observed binary phases are simulated using DFT.

Once the equilibrium energy for the various crystal structures are calculated, we evaluated the likelihood of the formation of each phase at 0K using the following formula for heat of formation:

$$\Delta H = \frac{E_{Equil} - N_X E_X^{Coh} - N_Y E_Y^{Coh}}{N_X + N_Y} \tag{0.3}$$

where E_{Equil} represents the total equilibrium energy of a binary compound with elements X and Y, E_X^{Coh} and E_Y^{Coh} are the cohesive energies of elements X and Y, respectively, in their stable bulk structures, and N_X and N_Y denotes the number of atoms of element X and Y in a binary structure. For a particular stochiometric ratio, the formation of the most stable phase is associated with the lowest heat of formation. A positive value for enthalpy of formation indicates that the reaction is endothermic while a negative value exhibits an exothermic reaction.

Table 1.5 and Table 1.6 detail the results of the heat of formation and equilibrium volume, respectively, evaluated by the binary MEAM potentials. Figure A.1 and Figure

A.2 in Appendix A can help visualize the relative order of the heats of formation for the element pair X – Y as a function of atomic percentage of element Y. Priority is given to accurately capture the heat of formation and equilibrium volume of the experimentally observed structures. The next step is to ensure, where applicable, that the experimentally observed structures are the most stable structures for their specific stochiometric ratio. Finally, effort is expended to maintain the relative order of formation of the hypothetical structures. As illustrated in Table 1.5, the maximum deviation of the heat of formation for the majority of experimentally observed structures is below 40%. The $D0_3$ structure of Fe – Si system is an exception, but the experimental compounds exhibit the correct order of formation. In addition, Table 1.6 indicates that most of the equilibrium volumes calculated by the MEAM potential are within 25% of the experimental or DFT observed values, with the exception of a Fe – Mn binary and a few other outliers. Since Mn does not form any experimental structures with Fe but rather tends to mix in the Fe bulk as a solid solution, the accuracy to capture the heat of formation and equilibrium volume was leveraged for substitutional formation energies. The heat of formation and equilibrium volume of the Mn – Si and Si – C binary compounds were not calibration objectives, and therefore, the Mn – Si and Si – C binary parameters are used as variables for calibrating the ternary.

Table 1.5 Heat of formation for binary compounds evaluated by MEAM potential in comparison to experimental and DFT results. The difference is w.r.t. experiment when available, otherwise DFT.

Binary System	Alloy Phase	Heat of Formation, ΔH (eV/atom)			
		MEAM	Exp.	DFT	% Diff.*
Fe – Mn	B1	1.8	-	0.88	105
	B2	1.6	-	0.36	344
	B3	3.1	-	1.26	146
	L12 (Fe_3Mn)	0.94	-	0.12	683
Fe – Si	B1	0.24	-	0.25	4
	B2	-0.16	-	-0.48	67
	B3	-0.31	-	0.71	143
	B20	-0.40	-0.41[a]	-0.50	2.4
	L12 (Fe_3Si)	0.47	-	-0.27	274
	$D0_3$ (Fe_3Si)	0.06	-0.21[a]	-0.32	129
Fe – C	B1	0.53	-	0.53	0
	B2	1.53	-	0.83	84
	B3	0.37	-	0.42	12
	Cementite	0.0485	0.0489[b]	0.01	0.8
	L12 (Fe_3C)	1.25	-	0.72	74
Mn – C	B1	0.51	-	0.36	42
	B2	0.83	-	0.68	22
	B3	3.95	-	0.38	939
	$Mn_{12}C_4$	-0.079	-0.103[c]	-0.107	22
	$Mn_{23}C_6$	-0.11	-0.111[c]	-0.11	0.9
	Mn_7C_3	-0.07	-0.111[c]	-0.107	38
	L12 (Mn_3C)	0.70	-	0.64	9.4

* Absolute value listed for % Difference

[a] Reference 41 as cited by [68]

[b] [69]

[c] Reference 10 as reported by [70]

Table 1.6 Equilibrium volume for binary compounds calculated using MEAM parameters in comparison to experimental and DFT values. The difference is w.r.t. experiment when available, otherwise DFT.

Binary System	Alloy Phase	Equilibrium Volume, V (Å^3)			
		MEAM	Exp.	DFT	% Diff.
Fe – Mn	B1	172	-	93.5	84
	B2	33.8	-	21.2	59
	B3	223.6	-	116.2	92
	L12 (Fe_3Mn)	61.4	-	41.4	48
Fe – Si	B1	106.5	-	104.5	1.9
	B2	22.8	-	21.1	8
	B3	137.4	-	140.6	2.3
	B20	90.1	89.9[a]	88.3	0.2
	L12 (Fe_3Si)	47	-	45.9	2.4
	$D0_3$ (Fe_3Si)	183.2	180.3[a]	182.2	1.6
Fe – C	B1	63.5	-	63.6	0.2
	B2	14.9	-	14.9	0
	B3	78.1	-	77.1	1.3
	Cementite	154	154.3[b]	151.6	0.2
	L12 (Fe_3C)	37.5	-	39.2	4.3
Mn – C	B1	79.1	-	65.0	22
	B2	16.9	-	15.2	11
	B3	144.9	-	82.3	76
	$Mn_{12}C_4$	162.2	157.4[c]	148.9	3.1
	$Mn_{23}C_6$	1272	1189[d]	1118	7.0
	Mn_7C_3	418.8	378.3[d]	354.7	11
	L12 (Mn_3C)	39.1	-	38.8	0.8

[a] [71]

[b] [72]

[c] [73]

[d] [74]

1.3.2 Elastic Constants for the Binary Structures

The MEAM potential parameters are adjusted to ensure that the binary compounds, especially those experimentally observed, are mechanically stable using the elastic moduli.

The alpha (X,Y) MEAM parameter was primarily used to calibrate the bulk modulus. For non-cubic orthogonal structures such as cementite, $Mn_{12}C_4$, and Mn_7C_3, the bulk (B) and shear moduli (C' and C_{44}^*) are evaluated as following

$$B = \frac{C_{11}+C_{22}+C_{33}+2(C_{12}+C_{13}+C_{23})}{9} \quad (0.4)$$

$$C' = \frac{C_{11}+C_{22}+C_{33}-C_{12}-C_{13}-C_{23}}{6} \quad (0.5)$$

$$C_{44}^* = \frac{C_{44}+C_{55}+C_{66}}{3} \quad (0.6)$$

where C_{44}^* is the average of the three shear components C_{44}, C_{55}, and C_{66}.

Table 1.7 lists the results of the elastic constants obtained for experimental and hypothetical phases. As indicated, the maximum deviation of the elastic moduli predicted by MEAM potential is within 80% of the experimental or DFT results.

Table 1.7 Elastic constants for binary compounds. Results calculated using MEAM potential are compared to experimental or literature results.

		Elastic Constants (GPa)						
		B		C′		C_{44}^*		
Binary System	Alloy Phase	MEAM	Exp. (DFT)	MEAM	Exp. (DFT)	MEAM	Exp. (DFT)	% Diff.
Fe – Mn	B2	289.8	(271)	24.6	(63)	269.9	(174)	41
Fe – Si	B20	78.7	110[a] (210)[b]	22.3	(150)[b]	57.7	(180)[b]	60
	$D0_3$	266	168[c]	103	38[c]	124.7	137[c]	79
Fe – C	Cementite	201.7	(351)[d]	99.4	(161)[d]	76	(94)[d]	33
Mn – C	$Mn_{12}C_4$	369.6	(311)[e]	202.5	(138)[e]	247.1	(132)[e]	51
	$Mn_{23}C_6$	334.9	(314)[e]	306.7	(133)[e]	233	(139)[e]	68
	Mn_7C_3	324.4	(323)[e]	314.7	(116)[e]	112.1	(105)[e]	59

% Difference calculated by averaging the percentage difference of B, C′, and C_{44} w.r.t. experimental or literature results.

[a] [75] as cited by [68]

[b] [76]

[c] Kötter *et al.* as cited by [77]

[d] DFT results by Jiang *et al.* [78]

[e] First-principles evaluation by Chong *et al.* [79]

1.3.3 Substitutional and Interstitial Formation Energy

The formation energy of a substitutional point defect, E_f^{Sub}, of type-Y atom in the bulk of type-X atoms is defined using the following formula

$$E_f^{Sub} = E_{Total} - E_{Bulk}\left(\frac{N-1}{N}\right) - E_Y^{Coh} \tag{0.7}$$

where *N* is the total number of atoms in the bulk of type-X atoms, E_{Bulk} is the total bulk energy for the most stable structure of type-X atom with N number of atoms, E_{Total} is the total energy evaluated of one type-Y atom substituted in the bulk of type-X atoms, and E_y^{Coh} is the cohesive energy of the most stable structure for element Y. The bulk dimensions of 5 × 5 × 5 and 3 × 3 × 3 primitive cells of BCC Fe are used in MEAM and DFT, respectively. Table 1.8 details the substitutional formation energies comparing the MEAM potential calibration to DFT results that are depicted within parentheses. Since the MEAM potential for low-alloy steels is being developed, replicating the substitutional point defect energies of the alloying elements Mn and Si in the Fe bulk is imperative. Additionally, the results indicate that a majority of the substitutional energies are in good agreement and reproduced the same sign as the DFT results. The Mn – Si and Si – C MEAM parameters

were used for ternary calibration and consequently resulted in large substitutional energies. Fe in Mn bulk was also at least an order of magnitude larger than the DFT results.

Table 1.8 The formation energies of substitutional point defects for Fe, Mn, Si and C. Results obtained using DFT are presented in parenthesis while the MEAM potential values are reported without parenthesis.

	Substitutional 'Atom' Energy (eV)			
Host Atom	Fe	Mn	Si	C
Fe		0.057[a] (0.057)[b]	-1.286 (-1.28)	1.02 (2.95)
Mn*	10.4 (0.25)		22.6 (-0.98)	2.03 (2.54)
Si	2.80 (1.92)	10.8 (2.67)		12.7 (1.4)
C	8.64 (6.03)	5.25 (7.26)	17.1 (4.0)	

[a] Results produced by MEAM potential.

[b] DFT results in parenthesis.

* FCC used as bulk crystalline structure.

Having a much smaller atomic radius, carbon tends to alloy as an interstitial in Fe. Therefore, the formation energy of a carbon interstitial in an Fe bulk, E_f^{Int}, is evaluated using the following equation:

$$E_f^{Int} = E_{Total} - E_{Bulk} - E_C^{Coh} \tag{0.8}$$

where E_{Bulk} is the total bulk energy for BCC Fe atoms, E_{Total} is the total energy evaluated of one carbon atom located at an octahedral interstitial location in the bulk of Fe atoms, and E_C^{Coh} is the cohesive energy of the most stable structure for carbon. VASP calculations,

employing the same aforementioned bulk dimensions, predict the interstitial formation energy to be 0.36 eV versus the substitutional formation energy of 2.95 eV. The lower formation energy indicates that carbon is more stable as an interstitial than a substitution in Fe. The MEAM parameters also demonstrate the correct order of formation with the dilute interstitial solution energy as -1.62 eV whereas the dilute substitutional formation energy is 1.02 eV. Although MEAM potential predicted a negative interstitial formation energy for carbon in Fe, the difference of interstitial point defect with respect to substitutional point defect calculated by the MEAM potential (2.64 eV) with respect to VASP calculations (2.59 eV) remained consistent. The behavior that needs to be captured correctly, however, is the interaction of C with Mn and Si in the Fe bulk.

1.3.4 Ternary Substitutional and Interstitial Binding Energy

To calibrate the ternary potentials, the energy difference between having atoms of element Y and Z close together in the bulk of the most stable structure of element X versus having them far away is defined as the binding energy, E_{sub}^{BE}, and is evaluated as the following:

$$E_{sub}^{BE} = E_{Total}^{Y} + E_{Total}^{Z} - E_{Bulk}^{X} - E_{Total}^{Y-Z} \tag{0.9}$$

where E_{Total}^{Y-Z}, E_{Total}^{Y}, and E_{Total}^{Z} denote the total relaxed energy of Y and Z atoms, single Y atom, and single Z atom, respectively, in the bulk of element X. E_{Bulk}^{X} represents the total energy of a defect free element-X bulk. The binding energy will only be evaluated for Fe as the host atom while the pairs, Y – Z, will be located at the first (1NN) and second (2NN) nearest neighbor distances. Similar to the previous section, the bulk dimensions used for MEAM potential and DFT are consistent. Additionally, the binding energy of a

substitutional pair will only be presented for Mn – Si whereas the energy of a substitution-interstitial pairs will be evaluated for Mn – C and Si – C. A schematic of the 1NN and 2NN substitutional only and substitutional-interstitial pair is depicted in Figure 1.2. A substituted atom represented with a red (dotted outline) and blue (dashed outline) are located at the 1NN and 2NN locations with respect to the substitutional (gray) atom or the smaller (green) interstitial atom at the octahedral location.

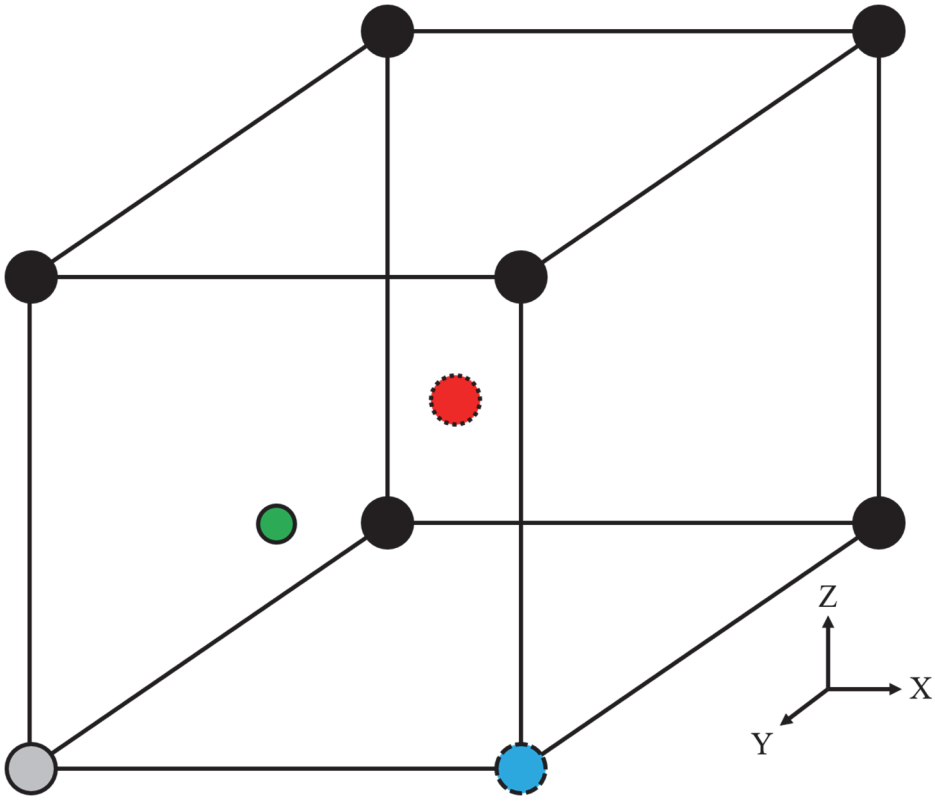

Figure 1.2 A schematic of the substituted atoms located 1NN (red, dotted) and 2NN (dashed, blue) with respect to another substituted atom (gray) or octahedral interstitial atom (green).

Table 1.9 lists the binding energies predicted by the MEAM parameters in comparison to the DFT values for the host Fe. Positive values of the binding energy denote a 'binding' or 'attractive' behavior whereas a negative number represents a 'repulsive'

trend. Results indicate that the MEAM potential values are in good agreement with the DFT values. Accurately capturing the interaction of the multicomponent system is a primary objective. We achieve this objective by constraining the formation of Mn – Si and Si – C binary compounds, and instead use the Mn – Si and Si – C binary interaction as an input variable to calibrate the ternary interaction. Furthermore, since Fe – Mn do not form any experimentally observed binary compounds, the pair potential is also calibrated such that it can capture both the binary substitutional formation energy and ternary binding energies.

Table 1.9 Ternary binding energies for substitutional pair of Mn-Si and substitution-interstitial pairs of Mn-C and Si-C in Fe bulk. The interaction of impurity pairs are evaluated at 1NN and 2NN. Results evaluated using DFT are represented in parenthesis whereas MEAM potential values are listed without parenthesis.

		Binding Energy (eV)		
		Substitutional Pair	Substitution – Interstitial Pair	
Host Atom	Pair Location	Mn – Si	Mn – C	Si – C
Fe	1NN	-0.14[a] (-0.14)[b]	-2.55 (-0.47)	-0.37 (-1.01)
	2NN	-0.67 (-0.17)	-0.17 (-0.60)	-0.88 (-1.25)

[a] Results produced by MEAM potential.

[b] DFT results in parenthesis.

1.4 Potential Validation Testing

The final step is to determine the applicability of the MEAM potential. A number of simulations were performed at finite temperatures to encapsulate the thermodynamic and kinetic properties of Fe and low-alloy steels. First, the coefficient of linear thermal expansion is evaluated for pure Fe using a 2000 atom system with periodic boundaries. The box was initially equilibrated using a NPT ensemble for 0.1 ns to achieve the correct zero pressure volume at a given temperature. A final equilibration was conducted for an interval of 1 ns, and the lattice dimensions were averaged over the time interval to calculate the linear thermal expansion coefficient. The same set of simulations was also used to evaluate the heat capacity of pure and alloyed iron. Table 1.10 and Table 1.11 compares the results of the coefficient of linear thermal expansion and heat capacity of iron of the MEAM potential results to the experimental results. At 300K, the linear thermal expansion and heat capacity for pure iron were within 4% of the experimentally observed values. Both the physical properties of the Fe alloys increased when doped with Mn and Si, demonstrating that the trend moved in the right direction but not as large as measured. Finally, the specific heat capacity and thermal expansion of a multicomponent low-alloy steel was evaluated, and the results indicated that the MEAM potential results were within 2.3% of experimental observations. A point of note is that the experimental agreement of heat capacity may also indicate that MD simulations provide results close to the Dulong-Petit law.

Table 1.10 Coefficient of linear thermal expansion evaluated for Fe at 300K using present MEAM potential and compared to experimental results.

	α_l at 300K (10^{-6} K^{-1})		
	MEAM	Experiment	% Difference
Fe	11.15	11.6[a]	3.9
Fe – 2% Mn	11.73	12.7[a,b]	7.6
Fe – 1% Si	11.48	12.2[a]	5.9
Fe – 1.25% Mn, 0.6% Si, 0.25% C	11.83	12.0[c]	1.4

[a] [80]

[b] Experimental value for Fe – 2.8% Mn.

[c] 1522 low-alloy steel [81]

Table 1.11 Heat capacity calculated for pure Fe and alloys at 300K. Results calculated using MEAM potential are compared to experimental observations.

	C_p at 300K (J g^{-1} K^{-1})		
	MEAM	Experiment	% Difference
Fe	0.467	0.4676[a]	0.12
Fe – 2% Mn	0.4709	0.5016[a]	6.12
Fe – 1% Si	0.4732	-	-
Fe – 1.25% Mn, 0.6% Si, 0.25% C	0.475	0.486[b]	2.3

[a] [82]

[b] 1522 low-alloy steel [81]

In addition, the self-diffusion coefficients were also evaluated for Fe using a single crystal comprising 16,000 atoms. The system was equilibrated using the NPT ensemble for 0.2 ns followed by an introduction of a small number of random vacancies. Finally, a canonical (NVT) ensemble was simulated for 1 ns where the atom positions were recorded every 500 fs. The atom position vectors are used to calculate the self-diffusion coefficients

using Einstein's formulation [83] relating mean square displacement as a function of observed time with the following equation

$$D = \frac{1}{2d} \lim_{t \to \infty} \frac{\langle [r(t_0+t) - r(t_0)]^2 \rangle}{t} \tag{0.10}$$

where d is the dimensionality of the system and the angled brackets signify that an ensemble average over all molecules and time origins must be considered. In order to observe diffusivity of atoms within a reasonable timeframe, an excess number of vacancy concentrations, C_v^{ex}, are introduced in the simulation environment. This requires the simulated diffusivity, D_{sim}, to be adjusted for the equilibrium vacancy concentration, C_v^{eq}. The actual diffusivity, D_{real}, of the system is then evaluated using the following equation

$$D_{real} = \frac{C_v^{eq}}{C_v^{ex}} D_{sim} \tag{0.11}$$

where the equilibrium vacancy concentration, C_v^{eq}, is obtained using:

$$C_v^{eq} = \exp\left[-\frac{H_f^v - TS_f^v}{k_B T}\right] \tag{0.12}$$

where H_f^v is the vacancy formation enthalpy, S_f^v is the vacancy formation entropy, and k_B is the Boltzmann constant. The vacancy formation entropy was taken from literature [84] as $2.20k_B$.

To evaluate uncertainty, each simulation is conducted three times with different seed numbers for the porosity and temperature, and 95 percent confidence intervals were employed for both temperature and the self-diffusion coefficients. Figure 1.3 shows that the MEAM potential calculated self-diffusion coefficients, with the diffusion activation energy of 0.11 eV, for pure Fe in comparison with the experimental results, having an activation energy of 0.18 eV [85].

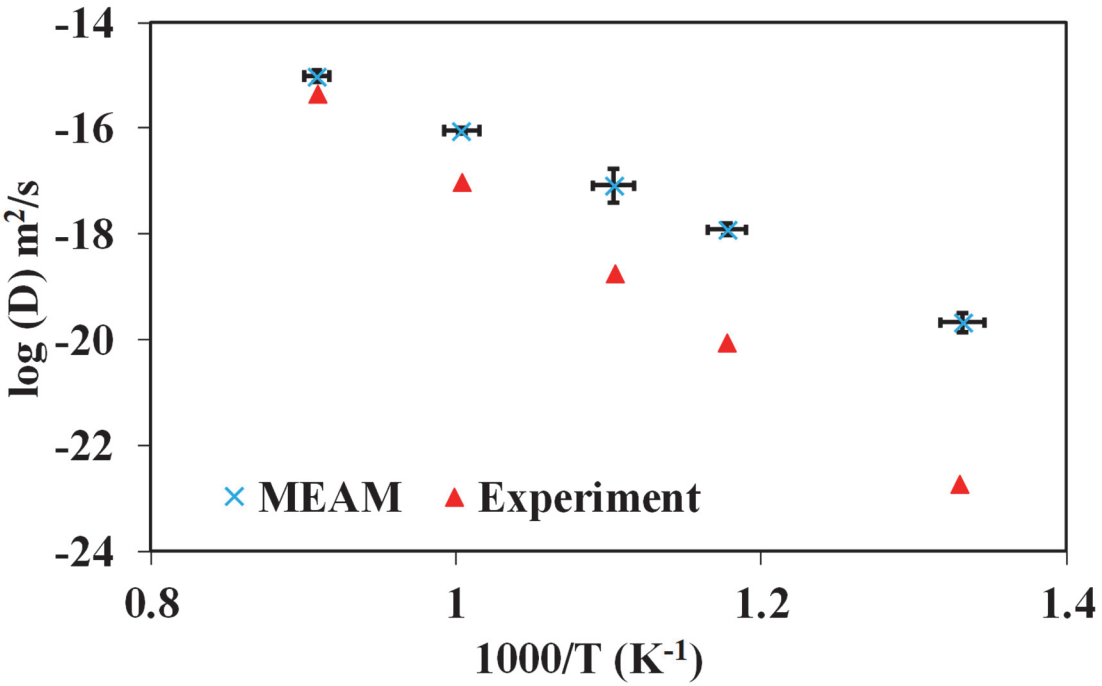

Figure 1.3 An Arrhenius plot of self-diffusion coefficients as a function of temperature. Results obtained by MEAM potential are in overall agreement with experimental values.

The binding energy of like-atoms at 1NN and 2NN locations is probed using the present MEAM potential and compared against the DFT calculations using the following equation:

$$E^{BE} = 2 \cdot E^{Y}_{Total} - E^{X}_{Bulk} - E^{Y-Y}_{Total} \tag{0.13}$$

where E^{Y}_{Total} and E^{Y-Y}_{Total} represent the total relaxed energy of a single Y and two Y atoms in Fe, respectively, in the bulk of element X. E^{X}_{Bulk} denotes the total relaxed energy of a defect free bulk of element X. The bulk dimensions used in Section 1.3.4 sets the precedent for the calculations of like-atom binding energies. The results from the analysis are summarized in Table 1.12 and Table 1.13.

Table 1.12 Binding energy of like-atoms at 1NN and 2NN for the substitutional pairs of Mn and Si in an Fe bulk. The calculation conducted using the present MEAM potential, presented without parenthesis, is compared to results obtained using DFT in parenthesis.

		Binding Energy (meV)	
		Substitutional Pair	
Host Atom	Pair Location	Mn – Mn	Si – Si
Fe	1NN	67[a] (-49)[b]	1765 (-152)
	2NN	262 (-87)	142 (-96)

[a] Results produced by MEAM potential.

[b] DFT results in parenthesis.

Table 1.13 Binding energies for the interstitial pairs of C (green) in the bulk of Fe (black). Results from the present MEAM potential are compared against the DFT calculations and corresponding literature study.

Atomic Structure	Binding Energy (meV)	
	C – C Interstitial Pair	
	Present Study	Literature [86]
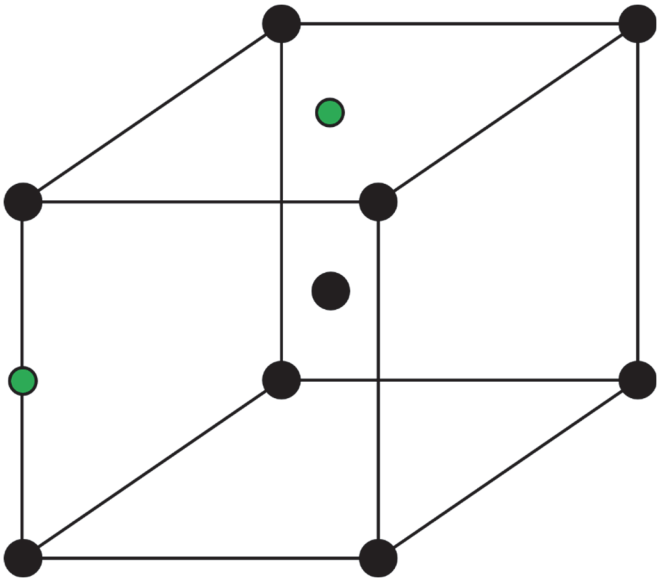	-511	-90
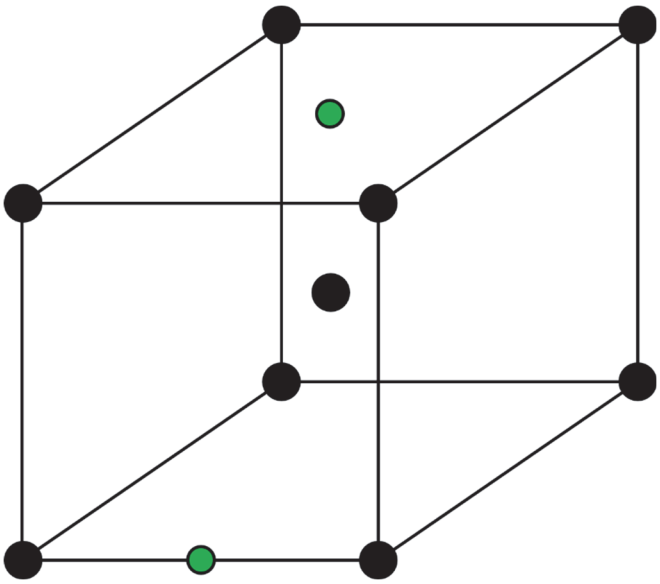	-165	130

1.5 Potential Prediction Testing

Since dislocation motion across a slip plane and in the slip direction is one of the possible mechanisms of plasticity in BCC Fe, we evaluate the change in energy as the stacking sequence of a perfect bulk single crystal is changed at 0K. Figure 1.4a details the Generalized Stacking Fault Energy (GSFE) as a function of the normalized displacement. A comparison of the GSFE curve for alternative slip planes and directions evaluated using the present MEAM potential against DFT data produced by Yan *et al*. [87] indicates agreement and the correct relative energies between the faults. Additionally, the effect of alloying elements on the stacking fault energy is evaluated for Mn, Si, C, and a multicomponent system, as depicted in Figure 1.4b. The addition of Mn and C increased the stacking fault energy with respect to pure Fe while the addition of Si caused the stacking fault energy to remain approximately the same as pure Fe. A multicomponent system exhibited a decrease in peak stacking fault energy as well.

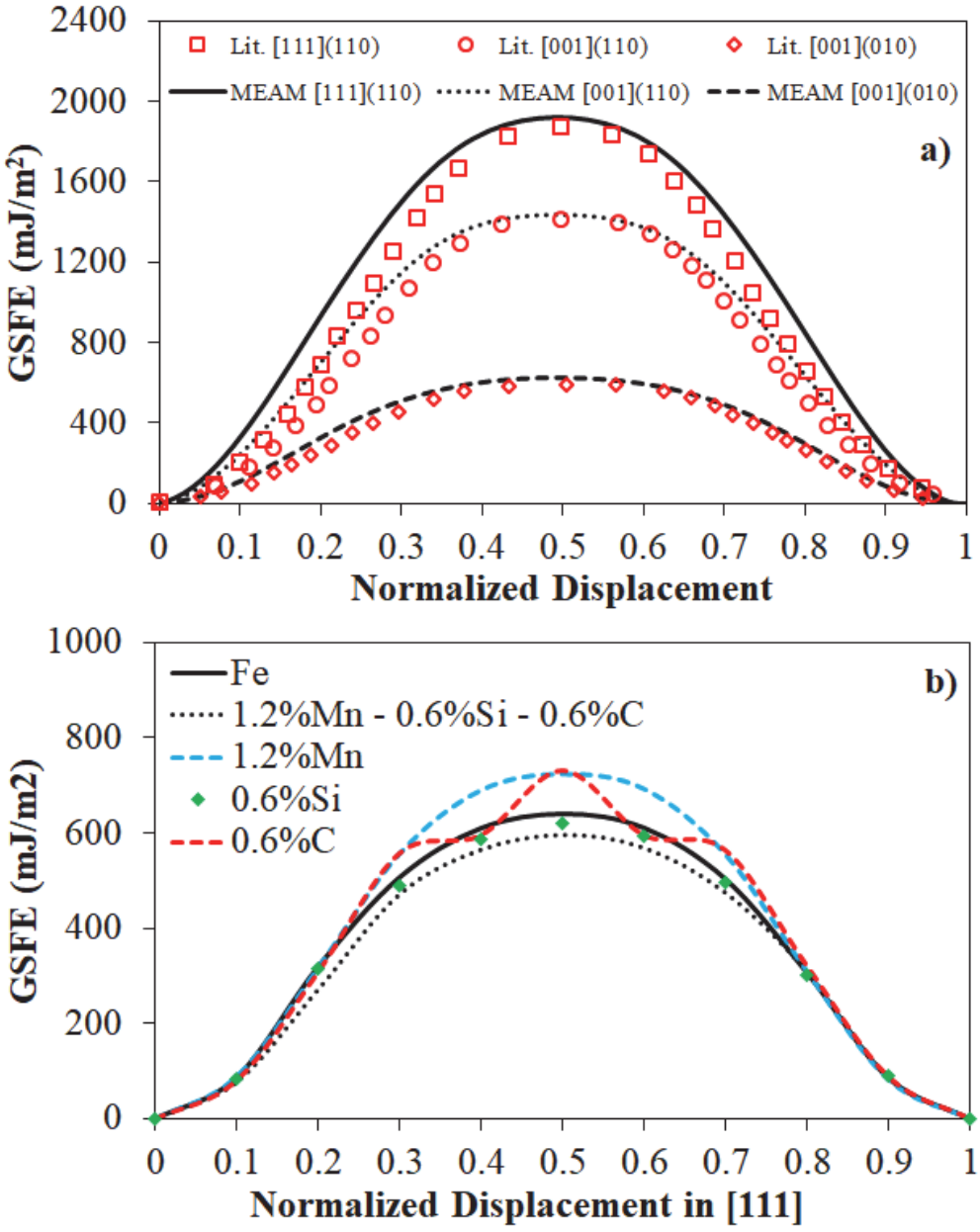

Figure 1.4 Generalized Stacking Fault Energy (GSFE) evaluated as a function of normalized displacement. a) GSFE obtained for multiple slip planes and directions evaluated using the present MEAM potential is compared against literature DFT of Fe. b) Effect of alloying element on the GSFE is evaluated and compared against the GSFE of pure Fe.

1.6 Conclusions

A quaternary element MEAM potential involving Fe, Mn, Si, and C was developed to simulate low-alloy steels using a hierarchical multiscale modeling paradigm. First, single element interatomic potentials were calibrated using experimental observations and first-principle calculations of the cohesive energy, lattice parameters, elastic constants, and point defect formation energies of vacancies and interstitials. Then, the calibration of binary element pairs was performed. This calibration entailed using the heat of formation, equilibrium volume, and elastic constants of binary compounds along with substitutional and interstitial formation energies as calibration targets. Finally, ternary interactions of Mn, Si, and C in Fe bulk were considered using substitutional and interstitial binding energies that were compared to *ab-initio* calculations.

A vital aspect of this atomistic study was to discern if the newly developed interatomic potentials could be applied to garner thermodynamic and kinetic data. Simulation results of the linear thermal expansion, heat capacity, and self-diffusion coefficients showed a great comparison to the experimental data found in the literature for Fe and its alloys, thereby extending confidence in the current MEAM potential to capture a wide array of atomistic phenomenon in a low-alloy steel.

1.7 Acknowledgements

This work was funded by the National Science Foundation (NSF) under contract number 1506878. M.A.Z. would like to acknowledge the funding support from NSF (CMMI-1507436 and CMMI-1911280) and ACS Petroleum Research Funds (55941-DNI10). The authors would also like to thank the Center for Advanced Vehicular Systems (CAVS) at Mississippi State University for supporting this work.

REFERENCES

[1] Z.G. Hu, P. Zhu, J. Meng, Fatigue properties of transformation-induced plasticity and dual-phase steels for auto-body lightweight: Experiment, modeling and application, Materials & Design. 31 (2010) 2884–2890. doi:10.1016/j.matdes.2009.12.034.

[2] J.V. Slycken, P. Verleysen, J. Degrieck, L. Samek, B.C. de Cooman, High-strain-rate behavior of low-alloy multiphase aluminum- and silicon-based transformation-induced plasticity steels, Metall and Mat Trans A. 37 (2006) 1527–1539. doi:10.1007/s11661-006-0097-8.

[3] R.O. Rocha, T.M.F. Melo, E.V. Pereloma, D.B. Santos, Microstructural evolution at the initial stages of continuous annealing of cold rolled dual-phase steel, Materials Science and Engineering: A. 391 (2005) 296–304. doi:10.1016/j.msea.2004.08.081.

[4] M. Sarwar, R. Priestner, Influence of ferrite-martensite microstructural morphology on tensile properties of dual-phase steel, JOURNAL OF MATERIALS SCIENCE. 31 (1996) 2091–2095. doi:10.1007/BF00356631.

[5] D. Bhattacharya, Developments in advanced high strength steels, in: The Joint International Conference of HSLA Steels, 2005: pp. 70–73.

[6] J. Coryell, J. Campbell, V. Savic, J. Bradley, S. Mishra, S. Tiwari, L.H. Jr, Tensile Deformation of Quenched and Partitioned Steel – A Third Generation High Strength Steel, in: Supplemental Proceedings, Wiley-Blackwell, 2012: pp. 555–562. doi:10.1002/9781118357002.ch70.

[7] S. Pisarik, D.V. Aken, K. Limmer, J. Medvedeva, Developing a Third-Generation Advanced High-Strength Steel with Two-Stage Trip Behavior, AISTech - Iron and Steel Technology Conference Proceedings. (2014) 3013–3023.

[8] G. Zheng, X. Li, Y. Chang, C. Wang, H. Dong, A Comparative Study on Formability of the Third-Generation Automotive Medium-Mn Steel and 22MnB5 Steel, J. of Materi Eng and Perform. 27 (2018) 530–540. doi:10.1007/s11665-018-3183-3.

[9] Y. Chang, S. Han, X. Li, C. Wang, G. Zheng, H. Dong, Effect of shearing clearance on formability of sheared edge of the third-generation automotive medium-Mn steel with metastable austenite, Journal of Materials Processing Technology. 259 (2018) 216–227. doi:10.1016/j.jmatprotec.2018.04.038.

[10] D.K. Matlock, J.G. Speer, Processing Opportunities for New Advanced High-Strength Sheet Steels, Materials and Manufacturing Processes. 25 (2010) 7–13. doi:10.1080/10426910903158272.

[11] L. Wang, J.G. Speer, Quenching and Partitioning Steel Heat Treatment, Metallogr. Microstruct. Anal. 2 (2013) 268–281. doi:10.1007/s13632-013-0082-8.

[12] M.F. Horstemeyer, Integrated computational materials engineering (ICME) for metals: using multiscale modeling to invigorate engineering design with science, WILEY [u.a.], Hoboken, NJ, 2012.

[13] V. Savic, L. Hector, H. Singh, M. Paramasuwom, U. Basu, A. Basudhar, N. Stander, Integrated Computational Materials Engineering Approach to Development of a Lightweight Third Generation Advanced High-Strength Steel (3GAHSS) Vehicle Body Structure, in: 2018. doi:10.4271/2018-01-1026.

[14] M.S. Daw, M.I. Baskes, Semiempirical, Quantum Mechanical Calculation of Hydrogen Embrittlement in Metals, Phys. Rev. Lett. 50 (1983) 1285–1288. doi:10.1103/PhysRevLett.50.1285.

[15] M.S. Daw, M.I. Baskes, Embedded-atom method: Derivation and application to impurities, surfaces, and other defects in metals, Phys. Rev. B. 29 (1984) 6443–6453. doi:10.1103/PhysRevB.29.6443.

[16] M.I. Baskes, Application of the Embedded-Atom Method to Covalent Materials: A Semiempirical Potential for Silicon, Phys. Rev. Lett. 59 (1987) 2666–2669. doi:10.1103/PhysRevLett.59.2666.

[17] M.S. Daw, Model of metallic cohesion: The embedded-atom method, Phys. Rev. B. 39 (1989) 7441–7452. doi:10.1103/PhysRevB.39.7441.

[18] M.I. Baskes, Modified embedded-atom potentials for cubic materials and impurities, Physical Review B. 46 (1992) 2727–2742. doi:10.1103/PhysRevB.46.2727.

[19] M.I. Baskes, J.E. Angelo, C.L. Bisson, Atomistic calculations of composite interfaces, Modelling Simul. Mater. Sci. Eng. 2 (1994) 505. doi:10.1088/0965-0393/2/3A/006.

[20] K. Gall, M.F. Horstemeyer, M. Van Schilfgaarde, M.I. Baskes, Atomistic simulations on the tensile debonding of an aluminum–silicon interface, Journal of the Mechanics and Physics of Solids. 48 (2000) 2183–2212. doi:10.1016/S0022-5096(99)00086-1.

[21] B.-J. Lee, M.I. Baskes, Second nearest-neighbor modified embedded-atom-method potential, Physical Review B. 62 (2000) 8564–8567. doi:10.1103/PhysRevB.62.8564.

[22] B.-J. Lee, M.I. Baskes, H. Kim, Y. Koo Cho, Second nearest-neighbor modified embedded atom method potentials for bcc transition metals, Phys. Rev. B. 64 (2001) 184102. doi:10.1103/PhysRevB.64.184102.

[23] E. Asadi, M. Asle Zaeem, S. Nouranian, M.I. Baskes, Quantitative modeling of the equilibration of two-phase solid-liquid Fe by atomistic simulations on diffusive time scales, Phys. Rev. B. 91 (2015) 024105. doi:10.1103/PhysRevB.91.024105.

[24] E. Asadi, M.A. Zaeem, M.I. Baskes, Phase-Field Crystal Model for Fe Connected to MEAM Molecular Dynamics Simulations, JOM. 66 (2014) 429–436. doi:10.1007/s11837-013-0845-3.

[25] B.-J. Lee, J.-H. Shim, M.I. Baskes, Semiempirical atomic potentials for the fcc metals Cu, Ag, Au, Ni, Pd, Pt, Al, and Pb based on first and second nearest-neighbor modified embedded atom method, Phys. Rev. B. 68 (2003) 144112. doi:10.1103/PhysRevB.68.144112.

[26] E. Asadi, M. Asle Zaeem, S. Nouranian, M.I. Baskes, Two-phase solid–liquid coexistence of Ni, Cu, and Al by molecular dynamics simulations using the modified embedded-atom method, Acta Materialia. 86 (2015) 169–181. doi:10.1016/j.actamat.2014.12.010.

[27] Y.-M. Kim, B.-J. Lee, M.I. Baskes, Modified embedded-atom method interatomic potentials for Ti and Zr, Phys. Rev. B. 74 (2006) 014101. doi:10.1103/PhysRevB.74.014101.

[28] Y.-M. Kim, N.J. Kim, B.-J. Lee, Atomistic Modeling of pure Mg and Mg–Al systems, Calphad. 33 (2009) 650–657. doi:10.1016/j.calphad.2009.07.004.

[29] D.E. Dickel, M.I. Baskes, I. Aslam, C.D. Barrett, New interatomic potential for Mg–Al–Zn alloys with specific application to dilute Mg-based alloys, Modelling and Simulation in Materials Science and Engineering. 26 (2018) 045010. doi:10.1088/1361-651X/aabaad.

[30] H.-S. Jang, K.-M. Kim, B.-J. Lee, Modified embedded-atom method interatomic potentials for pure Zn and Mg-Zn binary system, Calphad. 60 (2018) 200–207. doi:10.1016/j.calphad.2018.01.003.

[31] E. Asadi, M. Asle Zaeem, The anisotropy of hexagonal close-packed and liquid interface free energy using molecular dynamics simulations based on modified embedded-atom method, Acta Materialia. 107 (2016) 337–344. doi:10.1016/j.actamat.2016.01.043.

[32] Y.-M. Kim, Y.-H. Shin, B.-J. Lee, Modified embedded-atom method interatomic potentials for pure Mn and the Fe–Mn system, Acta Materialia. 57 (2009) 474–482. doi:10.1016/j.actamat.2008.09.031.

[33] B.-J. Lee, J.W. Lee, A modified embedded atom method interatomic potential for carbon, Calphad. 29 (2005) 7–16. doi:10.1016/j.calphad.2005.02.003.

[34] B.-J. Lee, A modified embedded atom method interatomic potential for silicon, Calphad. 31 (2007) 95–104. doi:10.1016/j.calphad.2006.10.002.

[35] E.H. Kim, Y.-H. Shin, B.-J. Lee, A modified embedded-atom method interatomic potential for Germanium, Calphad. 32 (2008) 34–42. doi:10.1016/j.calphad.2007.12.003.

[36] B.-J. Lee, J.-W. Jang, A modified embedded-atom method interatomic potential for the Fe–H system, Acta Materialia. 55 (2007) 6779–6788. doi:10.1016/j.actamat.2007.08.041.

[37] B.-J. Lee, T.-H. Lee, S.-J. Kim, A modified embedded-atom method interatomic potential for the Fe–N system: A comparative study with the Fe–C system, Acta Materialia. 54 (2006) 4597–4607. doi:10.1016/j.actamat.2006.06.003.

[38] T.S. Gates, G.M. Odegard, S.J.V. Frankland, T.C. Clancy, Computational materials: Multi-scale modeling and simulation of nanostructured materials, Composites Science and Technology. 65 (2005) 2416–2434. doi:10.1016/j.compscitech.2005.06.009.

[39] B.-J. Lee, A modified embedded-atom method interatomic potential for the Fe–C system, Acta Materialia. 54 (2006) 701–711. doi:10.1016/j.actamat.2005.09.034.

[40] C. Wu, B.-J. Lee, X. Su, Modified embedded-atom interatomic potential for Fe-Ni, Cr-Ni and Fe-Cr-Ni systems, Calphad. 57 (2017) 98–106. doi:10.1016/j.calphad.2017.03.007.

[41] P. Liu, X. Han, D. Sun, Q. Wang, Development and application of a ternary Ti-Al-N interatomic potential for Ti2AlN/TiAl composite, Journal of Alloys and Compounds. 745 (2018) 63–74. doi:10.1016/j.jallcom.2018.02.168.

[42] H.-K. Kim, W.-S. Jung, B.-J. Lee, Modified embedded-atom method interatomic potentials for the Fe–Ti–C and Fe–Ti–N ternary systems, Acta Materialia. 57 (2009) 3140–3147. doi:10.1016/j.actamat.2009.03.019.

[43] C.-L. Kuo, P. Clancy, Development of atomistic MEAM potentials for the silicon–oxygen–gold ternary system, Modelling Simul. Mater. Sci. Eng. 13 (2005) 1309. doi:10.1088/0965-0393/13/8/008.

[44] C.A. Becker, F. Tavazza, Z.T. Trautt, R.A. Buarque de Macedo, Considerations for choosing and using force fields and interatomic potentials in materials science and engineering, Current Opinion in Solid State and Materials Science. 17 (2013) 277–283. doi:10.1016/j.cossms.2013.10.001.

[45] B. Jelinek, S. Groh, M.F. Horstemeyer, J. Houze, S.G. Kim, G.J. Wagner, A. Moitra, M.I. Baskes, Modified embedded atom method potential for Al, Si, Mg, Cu, and Fe alloys, Physical Review B. 85 (2012). doi:10.1103/PhysRevB.85.245102.

[46] M.F. Horstemeyer, Integrated Computational Materials Engineering (ICME) for Metals: Using Multiscale Modeling to Invigorate Engineering Design with Science, Wiley.Com. (n.d.).

[47] J.P. Perdew, K. Burke, M. Ernzerhof, Generalized Gradient Approximation Made Simple, Physical Review Letters. 77 (1996) 3865–3868. doi:10.1103/PhysRevLett.77.3865.

[48] H.J. Monkhorst, J.D. Pack, Special points for Brillouin-zone integrations, (n.d.) 5.

[49] C.D. Barrett, R.L. Carino, The MEAM parameter calibration tool: an explicit methodology for hierarchical bridging between ab initio and atomistic scales, Integr Mater Manuf Innov. 5 (2016) 9. doi:10.1186/s40192-016-0051-6.

[50] R.L. Carino, M.F. Horstemeyer, Case Studies in Using MATLAB to Build Model Calibration Tools for Multiscale Modeling, in: J. Valdman (Ed.), Applications from Engineering with MATLAB Concepts, InTech, 2016. doi:10.5772/62348.

[51] C. Kittel, Introduction to Solid State Physics, 8th Edition, John Wiley & Sons, 2004.

[52] C.S. Barrett, T.B. Massalski, Structure of metals: crystallographic methods, principles and data, 3rd rev. ed, Pergamon, Oxford ; New York, 1980.

[53] S. Fahy, S.G. Louie, High-pressure structural and electronic properties of carbon, Phys. Rev. B. 36 (1987) 3373–3385. doi:10.1103/PhysRevB.36.3373.

[54] L. Brewer, Cohesive energies of the elements, California Univ., Berkeley (USA). Lawrence Berkeley Lab., 1975. doi:10.2172/7187973.

[55] H.-E. Schaefer, K. Maier, M. Weller, D. Herlach, A. Seeger, J. Diehl, Vacancy formation in iron investigated by positron annihilation in thermal equilibrium, Scripta Metallurgica. 11 (1977) 803–809. doi:10.1016/0036-9748(77)90079-5.

[56] S. Dannefaer, P. Mascher, D. Kerr, Monovacancy Formation Enthalpy in Silicon, Physical Review Letters. 56 (1986) 2195–2198. doi:10.1103/PhysRevLett.56.2195.

[57] M. Timonova, B.-J. Lee, B.J. Thijsse, Sputter erosion of Si(001) using a new silicon MEAM potential and different thermostats, Nuclear Instruments and Methods in Physics Research Section B: Beam Interactions with Materials and Atoms. 255 (2007) 195–201. doi:10.1016/j.nimb.2006.11.023.

[58] S. Ryu, C.R. Weinberger, M.I. Baskes, W. Cai, Improved modified embedded-atom method potentials for gold and silicon, Modelling and Simulation in Materials Science and Engineering. 17 (2009) 075008. doi:10.1088/0965-0393/17/7/075008.

[59] P. Torelli, F. Sirotti, P. Ballone, Surface alloying and mixing at the Mn/Fe(001) interface: Real-time photoelectron spectroscopy and modified embedded atom simulations, Physical Review B. 68 (2003). doi:10.1103/PhysRevB.68.205413.

[60] F.R. de Boer, Cohesion in metals: transition metal alloys, North-Holland ; Sole distributors for the U.S.A. and Canada, Elsevier Scientific Pub. Co., Amsterdam ; New York : New York, N.Y., U.S.A., 1988. https://catalog.hathitrust.org/Record/001551517 (accessed May 16, 2018).

[61] M. Rosen, Elastic Moduli and Ultrasonic Attenuation of Polycrystalline α-Mn from 4.2-300°K, Phys. Rev. 165 (1968) 357–359. doi:10.1103/PhysRev.165.357.

[62] K. Takemura, O. Shimomura, K. Hase, T. Kikegawa, The high-pressure equation of state of α-Mn to 42 GPa, J. Phys. F: Met. Phys. 18 (1988) 197. doi:10.1088/0305-4608/18/2/004.

[63] N. Mōri, M. Takahashi, G. Oomi, Magnetic contribution to the bulk modulus of 3d-transition metal alloys, Journal of Magnetism and Magnetic Materials. 31–34 (1983) 135–136. doi:10.1016/0304-8853(83)90187-7.

[64] H. Fujihisa, K. Takemura, Stability and the equation of state of alpha-manganese under ultrahigh pressure, Phys. Rev. B. 52 (1995) 13257–13260. doi:10.1103/PhysRevB.52.13257.

[65] A. Dargys, J. Kundrotas, Handbook on physical properties of Ge, Si, GaAs and InP, Science and Encyclopedia Publ, Vilnius, 1994.

[66] M.H. Grimsditch, A.K. Ramdas, Brillouin scattering in diamond, Phys. Rev. B. 11 (1975) 3139–3148. doi:10.1103/PhysRevB.11.3139.

[67] S. Mun, A.L. Bowman, S. Nouranian, S.R. Gwaltney, M.I. Baskes, M.F. Horstemeyer, Interatomic Potential for Hydrocarbons on the Basis of the Modified Embedded-Atom Method with Bond Order (MEAM-BO), J. Phys. Chem. A. 121 (2017) 1502–1524. doi:10.1021/acs.jpca.6b11343.

[68] E.G. Moroni, W. Wolf, J. Hafner, R. Podloucky, Cohesive, structural, and electronic properties of Fe-Si compounds, Phys. Rev. B. 59 (1999) 12860–12871. doi:10.1103/PhysRevB.59.12860.

[69] S.V. Meschel, O.J. Kleppa, Standard enthalpies of formation of some 3d transition metal carbides by high temperature reaction calorimetry, Journal of Alloys and Compounds. 257 (1997) 227–233. doi:10.1016/S0925-8388(97)00023-6.

[70] D. Djurovic, B. Hallstedt, J. von Appen, R. Dronskowski, Thermodynamic assessment of the Mn–C system, Calphad. 34 (2010) 279–285. doi:10.1016/j.calphad.2010.05.002.

[71] P. Paufler, P. Villars, L. D. Calvert. Pearson's handbook of crystallographic data for intermetallic phases. American Society for Metals. Metals Park. Ohio. 1986. Vols. 1–3. 3258 pp, US $ 495.00 ISBN 0-87170-217-7, Crystal Research and Technology. 22 (n.d.) 1436–1436. doi:10.1002/crat.2170221117.

[72] I.G. Wood, L. Vočadlo, K.S. Knight, D.P. Dobson, W.G. Marshall, G.D. Price, J. Brodholt, Thermal expansion and crystal structure of cementite, Fe 3 C, between 4 and 600 K determined by time-of-flight neutron powder diffraction, Journal of Applied Crystallography. 37 (2004) 82–90. doi:10.1107/S0021889803024695.

[73] J. Bouchaud, Etude structurale des carbures de manganese, in: Annales de Chimie, 1967: pp. 353–366.

[74] P. Karen, H. Fjellvåg, A. Kjekshus, A.F. Andresen, On the phase relations and structural and magnetic properties of the stable manganese carbides Mn23C6, Mn5C2 and Mn7C3, Acta Chemica Scandinavica. 45 (1991) 549–557.

[75] G.P. Zinoveva, L.P. Andreeva, P.V. Geld, Elastic constants and dynamics of crystal lattice in monosilicides with B20 structure, Physica Status Solidi (A). 23 (n.d.) 711–718. doi:10.1002/pssa.2210230244.

[76] R. Caracas, R. Wentzcovitch, Equation of state and elasticity of FeSi, Geophysical Research Letters. 31 (n.d.). doi:10.1029/2004GL020601.

[77] G. Randltt, Lattice dynamics and related diffusion properties of intermetallics: I. Fe3Si, (n.d.) 18.

[78] C. Jiang, S.G. Srinivasan, A. Caro, S.A. Maloy, Structural, elastic, and electronic properties of Fe3C from first principles, Journal of Applied Physics. 103 (2008) 043502. doi:10.1063/1.2884529.

[79] X. Chong, Y. Jiang, R. Zhou, J. Feng, First principles study the stability, mechanical and electronic properties of manganese carbides, Computational Materials Science. 87 (2014) 19–25. doi:10.1016/j.commatsci.2014.01.054.

[80] Dwight E. Gray (Ed.), American Institute of Physics Handbook, McGraw-Hill Book Company Inc., 1957.

[81] ASM International, J.R. Davis, ASM International, eds., Properties and selection: irons, steels and high-performance alloys, [10. ed.], 6. print, ASM International, Materials Park, Ohio, 2001.

[82] V.T. Witusiewicz, F. Sommer, E.J. Mittemeijer, Enthalpy of formation and heat capacity of Fe-Mn alloys, Metall and Materi Trans B. 34 (2003) 209–223. doi:10.1007/s11663-003-0008-y.

[83] J.M. Haile, Molecular Dynamics Simulation: Elementary Methods, 1st ed., John Wiley & Sons, Inc., New York, NY, USA, 1992.

[84] J.J. Burton, Vacancy-Formation Entropy in Cubic Metals, Phys. Rev. B. 5 (1972) 2948–2957. doi:10.1103/PhysRevB.5.2948.

[85] B. Zhang, Calculation of self-diffusion coefficients in iron, AIP Advances. 4 (2014) 017128. doi:10.1063/1.4863462.

[86] C.S. Becquart, J.M. Raulot, G. Bencteux, C. Domain, M. Perez, S. Garruchet, H. Nguyen, Atomistic modeling of an Fe system with a small concentration of C, Computational Materials Science. 40 (2007) 119–129. doi:10.1016/j.commatsci.2006.11.005.

[87] J.-A. Yan, C.-Y. Wang, S.-Y. Wang, Generalized-stacking-fault energy and dislocation properties in bcc Fe: A first-principles study, Phys. Rev. B. 70 (2004) 174105. doi:10.1103/PhysRevB.70.174105.

APPENDIX A

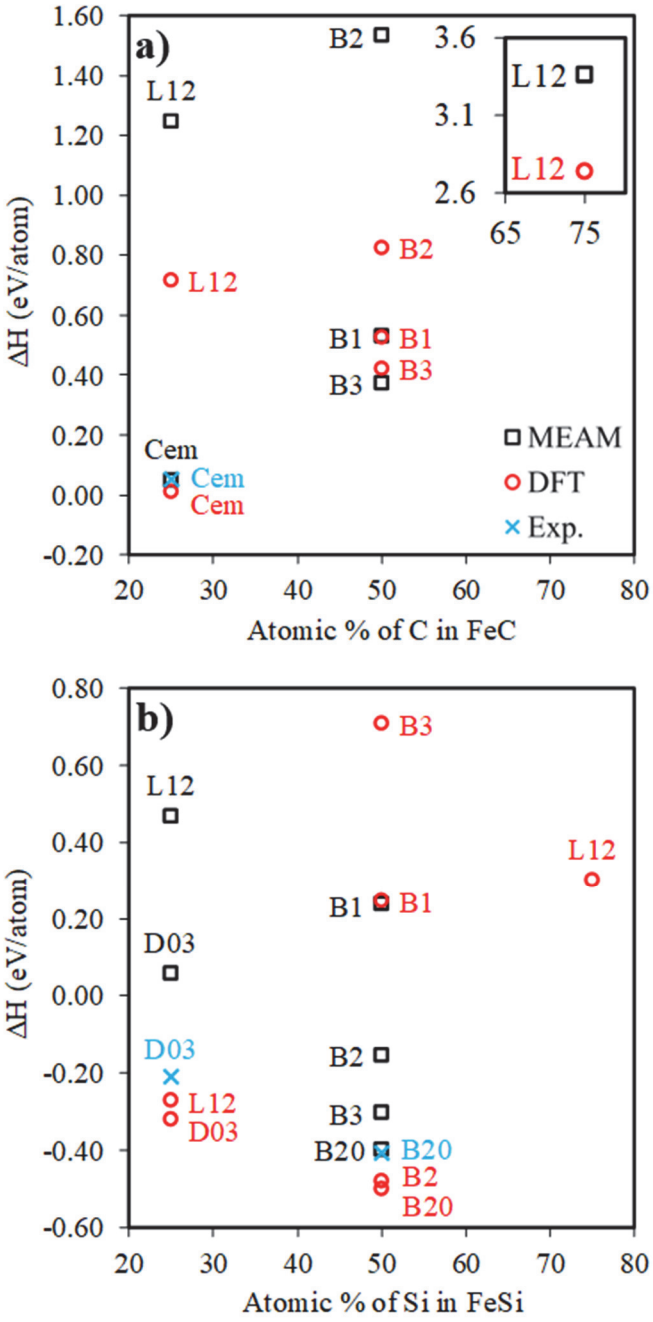

Figure A.1 Heat of formation for the binary compounds of a) Fe–C and b) Fe–Si plotted as a function of atomic percentage of an alloying element. The experimental structure for Fe–C is cementite.

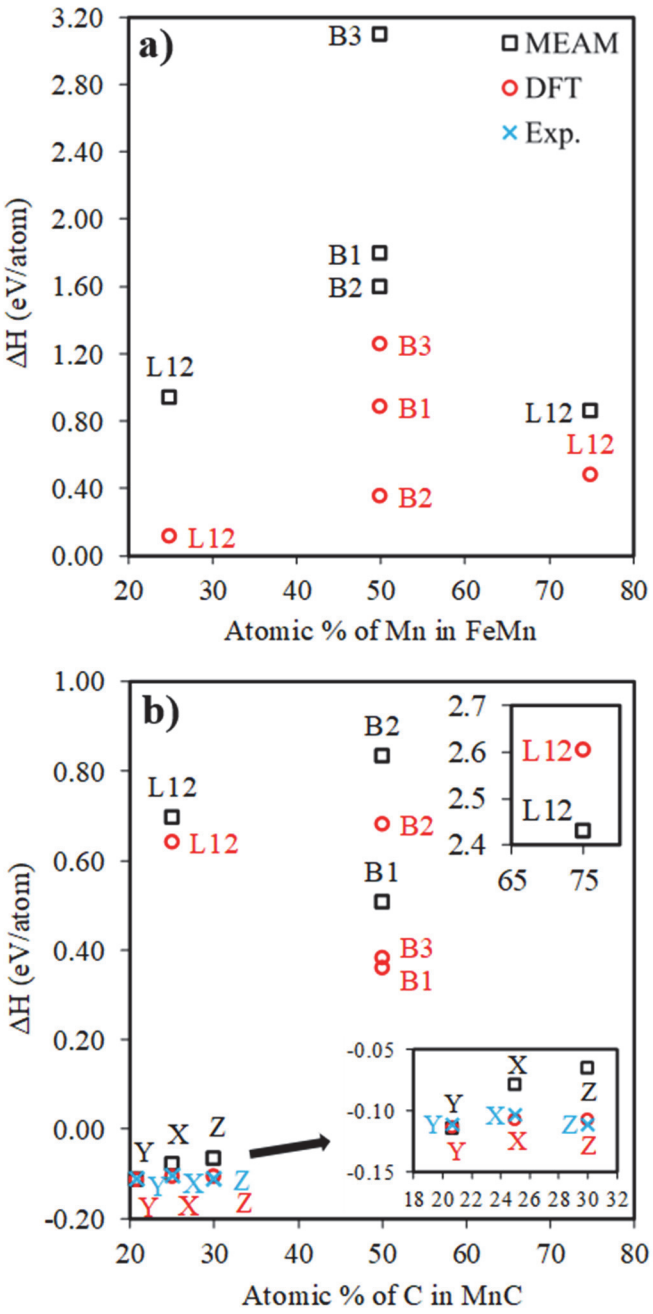

Figure A.2 Heat of formation for the binary compounds of a) Fe–Mn and b) Mn–C plotted as a function of atomic percentage of an alloying element. Compounds X, Y, and Z denote $Mn_{12}C_4$, $Mn_{23}C_6$, and Mn_7C_3, respectively.

APPENDIX B

Table B.1 MEAM potential parameters for Fe, Mn, Si, and C. E_c and a_{lat} have units of eV and Å.

	E_c	a_{lat}	α	A_{sub}	$\beta^{(0)}$	$\beta^{(1)}$	$\beta^{(2)}$	$\beta^{(3)}$	$t^{(1)}$	$t^{(2)}$	$t^{(3)}$	C_{min}	C_{max}	Attrac	Repuls
Fe	4.28	2.867	5.1	0.41	3.8	1.45	1.29	2.85	-5.118	9.12	-4	0.483	2.203	0	0.012
Mn	2.855	3.693	6.154	0.92	4.3	2.227	4.155	7.452	24	29.36	-4.897	2.4	0.19	0	0.032
Si	4.63	5.43	4.882	1	3.9	7	8.78	4.8	3.01	5.61	-0.6	2	2.8	0.12	0
C	7.346	3.567	4.382	1.2	2.55	2.2	1.0	3	3.246	7.496	-2.8	2	2.8	0.12	0

Table B.2 MEAM potential parameters for the binary pair (X – Y).

	Element Pair (X – Y)					
Parameters	Fe – Mn	Fe – Si	Fe – C	Mn – Si	Mn – C	Si – C
lattice (X,Y)	L12(X_3Y)	B1	B1	L12(X_3Y)	L12(X_3Y)	dia(B3)
R_e (X,Y)	2.79	2.37	1.995	4.654	2.393	1.888
E_c (X,Y)	3.002	4.22	5.285	0.34	3.382	0.34
Alpha (X,Y)	9.33	5.7	5.45	6.8	7.2	4.54
C^{max}_{X-X-Y}	2.82	1.98	2.7	2.8	2.5	2.8
C^{min}_{X-X-Y}	2.05	1	1.6	2	1	2
C^{max}_{Y-Y-X}	2.8	2.8	2.8	2.8	2.8	2.8
C^{min}_{Y-Y-X}	2	2	0.7	2	0	2
C^{max}_{X-Y-X}	2.8	2.8	2.8	2.8	2.8	2.8
C^{min}_{X-Y-X}	2	2	2	2	2	2
C^{max}_{X-Y-Y}	2.8	2.8	2.8	2.8	2.8	2.8
C^{min}_{X-Y-Y}	2	2	2	2	2	2
attrac (X,Y)	0	0	0	0	0	0
repuls (X,Y)	0	0.5	0.008	0	0.04	0
rho0 (X)	1	1	1	0.6	0.6	1.4
rho0 (Y)	0.6	1.4	4.4	1.4	4.4	4.4

Table B.3 MEAM potential parameters for the X – Y – Z ternary element interactions.

	Ternary Interactions (X – Y – Z)		
Parameters	Fe – Mn – Si	Fe – Mn – C	Fe – Si – C
C_{X-Y-Z}^{max}	2.8	1.2	2.8
C_{X-Y-Z}^{min}	2.0	0.29	2.0
C_{X-Z-Y}^{max}	2.8	2.8	2.8
C_{X-Z-Y}^{min}	2.0	2.0	2.0
C_{Y-Z-X}^{max}	2.8	2.8	2.8
C_{Y-Z-X}^{min}	2.0	2.0	2.0